Pore-scale computational analyses of non-Darcy flow through highly porous structures with various degrees of geometrical complexity

Hamid Moghimi[a], Majid Siavashi[a], Mohaddeseh Mousavi Nezhad[b*], Alberto Guadagnini[c]

[a] *Applied Multi-Phase Fluid Dynamics Lab., School of Mechanical Engineering, Iran University of Science and Technology, Tehran, Iran*
[b] *Warwick Center for Predictive Modelling, School of Engineering, the University of Warwick, Coventry, UK;*
m.mousavi-nezhad@warwick.ac.uk
[c] *Dipartimento di Ingegneria Civile e Ambientale, Politecnico di Milano, Milano, Italy*

Abstract

This study relies on pore-scale direct computations of velocity fields within the highly porous open-cell metal foams (OCF) characterized by differing geometrical attributes. The Navier-Stokes equations are solved across a suite of synthetically generated pore structures to assess relationships between attributes/patterns of the pore-scale flow field and OCF pore-structure. This study explores the effect of porosity and number of pores per inch (PPI) of the foam structures on the onset of non-Darcy flow, and values of Forchheimer coefficient and permeability of the system. The results show that the complexity of the pore flow patterns causes the onset of non-Darcy flow to occur at low values of Reynolds number (Re_k). The analyses encompass a wide range of values of Re_k corresponding to Darcy and non-Darcy flow regimes. The results suggest that permeability increases up to 30% by increasing porosity from 0.85 to 0.95, the corresponding onset of a non-Darcy flow regime taking place for $Re_k = 1.77$ and 1.44, respectively. Otherwise, a significant decrease of permeability is documented upon increasing the PPI value from 10 to 40, the corresponding onset of a non-Darcy flow regime taking place for $Re_k = 1.77$ and 0.28, respectively.

Keywords: pore-scale modeling; direct numerical simulation (DNS); highly porous structures; non-Darcy flow, Forchheimer regime; permeability.

Nomenclature

Symbols		Greek symbols	
g	gravity	β	Forchheimer (beta) coefficient
k^*	Dimensionless permeability	ε	Porosity
k_{app}	Apparent permeability	μ	Dynamic viscosity
$\boldsymbol{k_D}$	Darcy permeability tensor	ν	Kinematic viscosity
k_D	Darcy permeability along the main flow direction	ρ	Fluid density
$\boldsymbol{k_F}$	Forchheimer permeability tensor		
k_F	Forchheimer permeability along the main flow direction		
l	Length of the sample		
p	Pressure		
Re_k	Reynolds number (permeability base)		
Re_l	Reynolds number (sample length base)		
t	Time		
$\boldsymbol{U}$	Darcy velocity vector		
U	Darcy velocity in flow direction		
$\boldsymbol{u}_p$	Pore velocity vector		
u_p	Pore velocity in the main flow direction		
$\boldsymbol{x}$	Coordinate vector		
Δp	Pressure drop in flow direction		
∇p	pressure gradient over a given distance		

Acronyms

DNS	Direct numerical simulation
OCF	Open-cell foam
PDF	Probability density function
PPI	Pores per inch
REV	Representative elementary volume
WP	Weaire–Phelan

1. Introduction

Modeling flow and solute transport phenomena in porous media is key to a variety of engineering applications such as those associated with, e.g., the oil industry [1], heat transfer scenarios [2], nanotechnologies [3], or solute/chemical transport in environmental [4] and industrial settings [5 & 6]. Modeling techniques for simulating fluid flow through porous media range from those based on continuum-scale approaches to advanced high-resolution pore-scale analyses. In the context of the former approach, spatially averaged values of model parameters that are employed to describe flow are typically used, the effect of pore-scale fluctuations being embedded in these with various degrees of complexity. The latter approach is useful to shed light on the way the subtle effects of pore-scale mechanisms can be embedded in continuum-scale modeling of flow [7]. As such, these methods are complementary, results obtained from pore-scale approaches being valuable to quantify macro-scale features/patterns of flow such as, e.g., the onset of non-Darcy flow regimes and the associated governing parameters [8 & 9].

Computational studies focused on pore-scale simulation of flow across pore spaces and assessment of key features therein are typically grounded on two modeling strategies, i.e., (1) pore-network modeling and (2) direct numerical simulation (DNS) of flow [10]. Pore-network modeling is computationally efficient for the simulation of hydrodynamic processes and essentially relies on the generation of a ball-and-stick connected network to mimic a simplified form of the pore space [7]. DNS methods are usually employed in the context of analyses associated with three-dimensional imaged or synthetically generated pore spaces, a detailed formulation of equations governing flow and/or transport being then numerically solved to quantify pore-scale mechanisms. Blunt et al. [10] described various methods of pore-scale imaging of natural porous rocks and ensuing numerical modeling strategies and illustrated their relative merits and drawbacks. In some studies, quantities such as permeability and/or Forchheimer parameters have been evaluated across a wide range of flow regimes [11]. Bijeljic et al. [12] investigated the impact of non-Darcy flow conditions on non-Fickian solute transport features in low porosity geomaterials. Bijeljic et al. [13] analyze correlations between the heterogeneity of the porous domain and flow patterns across imaged rock samples. Muljadi et al. [14] employed pore-scale direct numerical simulations within a finite volume framework to simulate non-Darcy flow in low permeability rocks. These

authors consider three-dimensional (3D) X-ray imaged pore spaces and investigate the onset of non-Darcy flow regimes as well as their characterization through Forchheimer model parameters. El-Zehairy et al. [8] developed a pore network model to analyze the impact of the pore structure on the onset of inertial flow. Some studies are then devoted to assessing continuum-scale flow parameters under a variety of conditions, including variably saturated flow scenarios in heterogeneous porous media [15], and systems conceptualized through a dual domain approach [16]. Guo and Wang [17] analyzed tortuosity through numerical simulations of flow across three-dimensional porous media extracted from micro-computed tomography images of porous silicon carbide composite samples. Some studies used various numerical modeling methods like data driven machine learning [18], and surrogate modelling approach [19] for non-linearity analysis.

Detailed investigations of flow behavior across porous media of various degrees of complexity are also key in the context of heat transfer scenarios [20], and in the fields of environmental and industrial applications comprising, e.g., cooling of electronic components and underground storage practices. Recent numerical analyses in this context include, e.g., the works of Chamkha and Selimefendigil [21], who tackled free convection and ensuing heat transfer across a corrugated enclosure filled with a porous medium saturated with nanofluids, or Chamka et al. [22], who considered the effect of key flow parameters on heat transfer mechanisms taking place across a cavity filled with fluid and a porous material under the action of a rotating adiabatic cylinder.

Open-cell metal foams constitute a class of porous media characterized by a coherent structure of metal strings and high porosity (up to 0.98). These are made of a set of interwoven struts resulting in a complex pore structure with large contact surface between fluid and solid parts, which can favor enhancement of pore fluid flow complexity or heat exchange rates. An increased efficiency of the performance of the foams is typically associated with non-Darcy flow regimes, which are seen to emerge even in the presence of low Reynolds numbers (i.e., for low values of the macroscopic fluid flux). Thus, assessment of the factors controlling the transition of flow conditions in such media from Darcy to non-Darcian regimes are of critical importance for modern engineering applications. In this broad context, metal foams are extensively applied in engineered vessels which require given heat transfer capacity including, e.g., heat exchangers with high heat transfer potential [23], fuel cells [24], solar collectors [25], or thermal energy storage systems [26]. As such, porous media such as open-cell foams (OCF) can assist

sustainable development through optimization of their potential towards applications in the energy sector, including, e.g., improving heat transfer in heat exchangers, or further development of nanotechnologies, fuel cells, acoustic and magnetohydrodynamics applications, and water desalination.

Topin et al. [27] perform an experimental study considering several metal foams with differing characteristics (as rendered, e.g., through the number of pores-per-inch (PPI) and their porosity) to investigate the way permeability associated with a Darcy flow regime varies across the samples considered and to analyze the effect of fiber surface roughness on main flow patterns. In several studies focusing on metal foam samples, the effects of PPI and porosity on flow and heat transfer are investigated numerically upon considering Lattice-Boltzmann [28] and DNS ([29]) approaches. Bhattacharya et al. [30] provide a numerical study focused on the parameters exerting the highest effects on the pressure drop across aluminum metal foams with diverse PPIs (ranging from 5 to 40) and porosities (ranging between 0.90 and 0.97). These authors show that increasing porosity and decreasing PPI could contribute to increase permeability in metal foams under Darcy flow conditions. Other works related to open-cell metal foams include analyses on: the effect of porosity and sample size on the performance of foams in the context of thermal energy storage under non-Darcy flow regimes [31]; dispersion processes [32]; empirical correlations between hydrodynamic flow and heat transfer rates [33]; numerical simulations of flow and acoustic fields in three-dimensional synthetically generated pore spaces [34]; the use of elements of fractal theory to assess the impact of geometrical attributes of the medium on tortuosity, permeability, and effective thermal conductivity [35]. The analytical study of Yang et al. [36] show that permeability of open-cell foams could be formulated as a function of porosity and pore size, permeability significantly increasing with porosity.

Detailed studies on the effects of the pore structure of highly porous open-cell metal foams on inertial pore-scale flow regimes are still scarce, especially with reference to the assessment of the parameters associated with the Forchheimer model which is typically used to depict non-Darcy flow regimes at the continuum scale ([30], [37], [38].) Here, we rely on a DNS approach (as implemented through the OpenFOAM software, which is briefly described in Appendix A [39]) and present the results of a suite of computational pore-scale analyses on 12 samples of high porosity open-cell metal foams considering various combinations of values of porosity (i.e., 0.85, 0.90, and 0.95) and PPI (i.e., 10, 20,

30, and 40). In addition to the development of a stable DNS modeling framework based on the OpenFOAM platform with the capability to simulate scenarios related to open-cell metal foams with various degrees of geometrical complexities, distinctive elements of novelty of the study include detailed investigations documenting: (*i*) structural controls on the onset of a non-Darcy macro-scale flow regime and the assessment of the corresponding model parameters associated with various degrees of geometrical complexity of the metal foams; (*ii*) main traits of the flow field across a wide range of Reynolds numbers encompassing Darcy as well as non-Darcy marco-scale flow regimes, including (*iii*) detailed statistical analysis of the spatially heterogeneous pore-scale velocity field.

2. Materials and methods

The study is structured as described in the following. Section 2 is devoted to the illustration of the methodology employed for the generation of synthetic open-cell foam (OCF) samples and the numerical approach used to simulate fluid flow therein. The key results of the study are illustrated in Section 3. Finally, concluding remarks are provided in Section 4.

We analyze 12 open-cell foam samples which are synthetically generated to span various porosity and PPI values. Our suite of computational studies is aimed at characterizing key flow elements associated with foams, including, e.g., their permeability, the onset of a non-Darcy flow regime, and the Forchheimer coefficient, as a function of the above-mentioned system parameters. The main characteristics of the samples are listed in Table 1.

We note that the range of values of the geometrical parameters (porosity and PPI) employed for the generation of the synthetic media considered in our analyses is fully consistent with previous works and practical applications documented for open cell metal foam samples in various fields (e.g., [26] & [36]–[40]).

Boundary conditions used for the simulations are included in Fig. 1. A given pressure drop is set between the inlet and outlet boundaries, the remaining boundaries (including the external boundaries and the foam ligaments) are considered as impermeable walls characterized by a no-slip condition. Our computational analyses are performed for an extensive range of imposed pressure drops across the system (these ranging between 1×10^{-3} and 40×10^3 Pa/m) to comprise both Darcy and non-Darcy

macro-scale flow regimes. Main assumptions underlying the pore-scale simulations of flow include considering an incompressible and isothermal flow taking place across a non-deformable porous medium. The results illustrated in the following are complemented by those included in Appendix B, which provides an exemplary depiction of the pressure field associated with one of the samples analyzed, results of similar quality being obtained for all systems considered.

Table 1. Characteristics of the synthetically generated open-cell metal foam (OCF) samples.

Sample number	Porosity	Pores per inch (PPI)	Ligament diameter (mm)
1	0.85	10	0.381
2	0.85	20	0.192
3	0.85	30	0.133
4	0.85	40	0.096
5	0.90	10	0.280
6	0.90	20	0.140
7	0.90	30	0.901
8	0.90	40	0.070
9	0.95	10	0.192
10	0.95	20	0.095
11	0.95	30	0.063
12	0.95	40	0.048

(a)   (b)
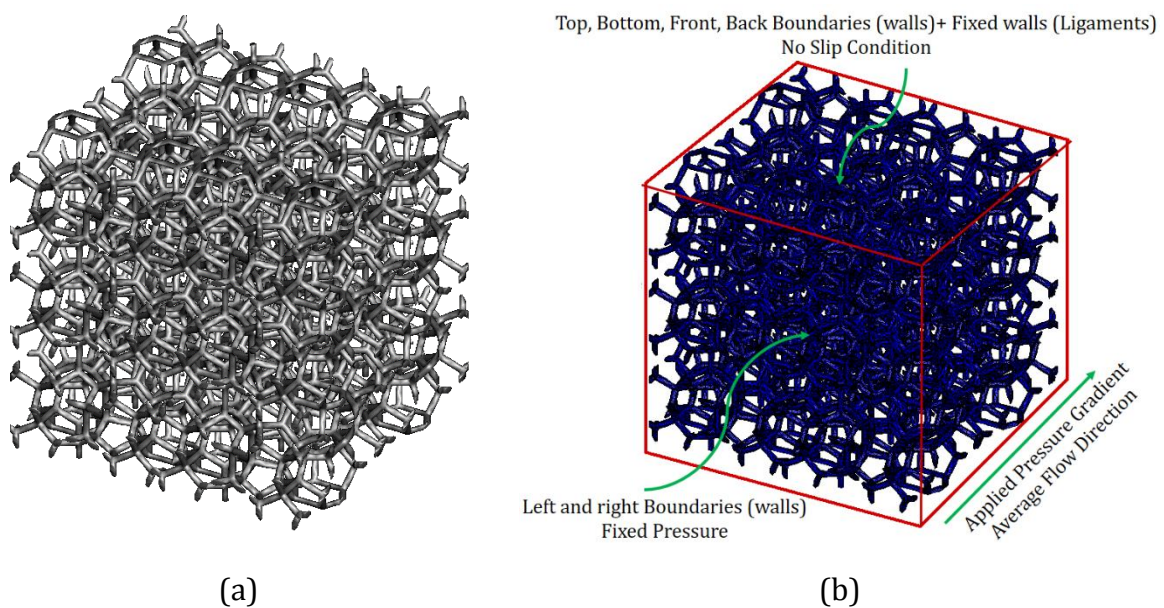
Fig. 1. Sketch of: (a) geometry, and (b) boundary conditions of a typical computational domain (corresponding to sample12 in Table 1).

The synthetic open-cell foam samples are generated using a typical surface evolver software [45]. There, an approach inspired to the surface energy minimization theory proposed by [46], which has been shown to be conducive to the generation of realistic pore structures typical of open-cell samples, is implemented. First, a number of similar unit cells forming a Weaire-Phelan (WP) structure are generated. These are then connected to yield the founding structure of the samples [46]. Internal mass and facets of the cells are then removed to form a porous structure associated with a given porosity and PPI values. Fig. 2 depicts a sketch of the process considered to generate the samples. The resulted porous samples are trimmed to form cubic three-dimensional open foam samples of a required size. PPI values typically range between 10 and 80. Foams associated with PPI= 10 are characterized by the largest void cells and simplest spatial structures. Foams with smaller void cells and a more complex spatial structures are generated by increasing values of PPIs. The ligament diameter is another important characteristic of foam structures. It typically decreases by increasing porosity, yielding sample structures with increased degree of complexity. OCF samples with different ligament diameters can be obtained upon varying porosity and PPI values.

Kelvin and WP unit cells are two geometrical basic structures that are typically employed to synthetically generate open-cell foam systems [35, 36]. The current study relies on a WP structure, which is based on two irregular dodecahedrons and six tetrakaidecahedrons that make it possible to generate highly complex foam structures [49]. It is noted that both Kelvin and WP structures are appropriate to generate foam structures similar to real foam samples. Otherwise, the WP structure enables one to generate foam structures with higher complexities (see, e.g., [49]). It is also noted that Cunsolo et al. [50] presented a comparison between pressure drop and friction factor results obtained by simulation of flow though synthetic samples generated by WP and Kelvin structures. Their numerical results showed that these approaches yield very similar distributions of pore pressure values and friction factors for samples associated with the same porosity. Considering (*a*) these results and (*b*) the additional benefit of relying on WP structures to obtain highly complex foam structures, we chose to synthesize our samples by the WP structure.
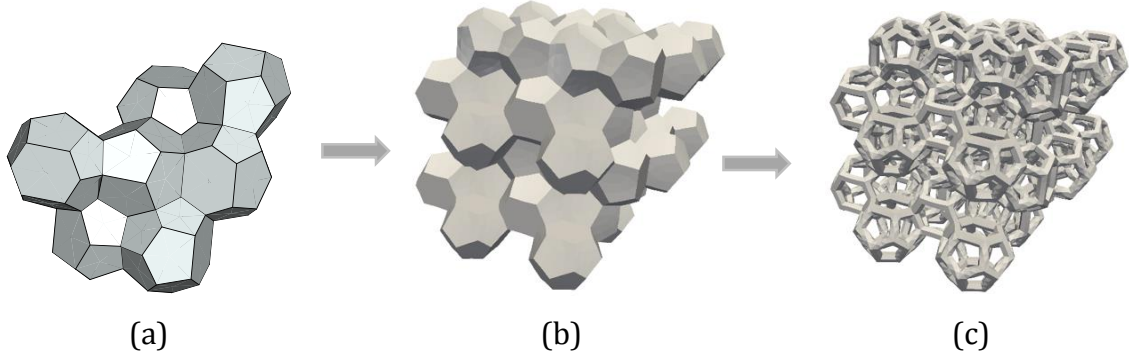
Fig. 2. Schematic representation of the procedure for the generation of the open-cell metal foam samples: (a) Weaire-Phelan structure; (b) main founding body of the samples; (c) final structure resulting after removal of mass and facets.

Steady-state incompressible fluid flow is described through mass conservation and upon relying on the direct numerical solution of the Navier-Stokes equations, i.e.,

$$\nabla.\boldsymbol{u}_p = 0 \tag{1}$$

$$(\boldsymbol{u}_p.\nabla)\boldsymbol{u}_p = -\frac{1}{\rho} \times \nabla p + \vartheta\nabla^2\boldsymbol{u}_p + g \tag{2}$$

where p and $\boldsymbol{u}_p$ represent pore fluid pressure and the velocity vector across the pore space, respectively; t represents time; ρ and ϑ denote (constant) fluid density and kinematic viscosity, respectively; and g is gravity.

The solution of these equations is obtained through an original steady-state solver implemented in the OpenFOAM platform using the SIMPLE (semi-implicit method for pressure linked equation) algorithm [39], which is one of the most widely used algorithms for solving Navier-Stokes equations resting on finite volume method. The solution strategy is based on a segregation approach, model outputs ($\boldsymbol{u}_p$ and p) being evaluated in a sequential manner. The calculated velocity and pressure distributions are then used to evaluate macro-scale hydrodynamic attributes of the porous structures, such as conductivity, tortuosity, and Forchheimer coefficient.

Darcy's Law is typically employed to describe continuum-scale flow across porous media upon neglecting non-linear flow behavior. Such a linear behavior is observed at very low velocity (or low values of the Reynolds number) and is expressed as:

$$-\nabla p = \frac{\mu}{\boldsymbol{k}_D}\boldsymbol{U} \tag{3}$$

where ∇p is pressure gradient, $\boldsymbol{U}$ is the Darcy velocity vector, $\boldsymbol{k}_D$ is the intrinsic permeability tensor of the porous domain, and μ is dynamic viscosity of the fluid.

A common modeling approach employed to characterize the documented non-linear relationship between Darcy velocity and pressure gradient arising as velocity (or Reynolds number) increases is based on the following Forchheimer equation [51]:

$$-\nabla p = \frac{\mu}{k_F} \boldsymbol{U} + \rho \beta U^2 \boldsymbol{n} \tag{4}$$

Here, β is a Forchheimer coefficient; U is the velocity norm; $\mathbf{n}$ is a unit vector in the direction of ∇p; and $\boldsymbol{k}_F$ represents a permeability tensor in the non-Darcy regime, which typically depends on velocity, as opposed to $\boldsymbol{k}_D$.

The onset of non-Darcy flow is deemed to take place when the relationship between pressure gradient and magnitude of U starts deviating from a linear behavior. Note that Equation (3) can be written as:

$$k_{ij} = \frac{\mu}{\nabla p_j} U_i \tag{5}$$

where ∇p_j and U_i are pressure gradient along direction j and Darcy velocity along direction i, respectively, k_{ij} being the corresponding entry in the permeability tensor. For simplicity, as we are only concerned with the permeability which contributes to the flow along the direction of an introduced pressure drop across the system, the Darcy velocity and permeability are hereafter denoted as U and k, respectively.

The Forchheimer coefficient β is typically estimated upon relying on experiments performed across a range of pressure gradient and flow values. By defining an apparent permeability:

$$k_{app} = l\mu \frac{U}{\Delta p} \tag{6}$$

where l is the length scale across which the pressure drop Δp is introduced, a linearized form of the Forchheimer equation can be written as [51]:

$$\frac{1}{k_{app}} = \frac{1}{k_F} + \beta \frac{\rho U}{\mu} \tag{7}$$

where k_F is the Forchheimer permeability along the main flow direction. Eq. 7 reveals a linear relation between $\frac{1}{k_{app}}$ and $\frac{\rho U}{\mu}$, which in turn enables a straightforward evaluation of β. A dimensionless permeability parameter k^* is then introduced as:

$$k^* = \frac{k_{app}}{k_D} \tag{8}$$

k_D corresponding to Darcy permeability along the main flow direction. It is typically assumed that the onset of the non-Darcy flow occurs at $k^* = 0.99$ [8].

A major focus is here on the statistical analysis of the Eulerian velocity fields stemming from the numerical simulations, consistent with the key aim of the study, which is geared towards the assessment of the emergence of (continuum-scale) flow regimes. As such, the statistics of the velocity fields associated with the geometrical attributes of the generated pore structures are characterized through the corresponding empirical frequency distributions and ensuing probability density functions. The degree of spatial correlation of the various velocity fields is then assessed through the evaluation of the sample variogram.

3. Results and discussion

The analysis starts by assessing the ability of the numerical approach developed in this study (see Section 2) to simulate macro-scale flow behavior encompassing Darcy and non-Darcy (i.e., Forchheimer) regimes through a detailed suite of computational analyses of flow taking place within the pore space associated with a Beadpack sample imaged via micro-CT. A detailed grid convergence study is performed to identify the optimal computational grids, details of the analysis being included in Appendix C. The effects of the generated pore structures mimicking open-cell metal foam samples (see Table 1) on the flow characteristics are then numerically assessed.

The computational code is benchmarked through comparison against a well-established scenario, which has been previously analyzed by Muljadi et al. [14] and El-Zehairy et al. [8]. These authors simulate flow across the pore space of an X-ray imaged Beadpack sample (depicted in Fig. 3). The sample is characterized by a porosity of 0.359 and the type of boundary conditions driving flow correspond to those described in Section 2. The computational results for hydraulic conductivity are listed in Table 2. These evidence that differences between hydraulic conductivity values stemming from our computational approach and those provided by Muljadi et al. [14] are less than 2.5%, thus imbuing us with confidence in the robustness of the computational approach here developed. Fig. 4 depicts the imposed pressure gradient across the sample versus the evaluated average flux, revealing a satisfactory agreement between our results and those of Muljadi et al. [14] and El-Zehairy et al. [8] across both Darcy (linear) and non-Darcy (non-linear) regimes. As described in [8], the point at which the pressure drop due to the linear term becomes less than 0.99 of the total pressure drop is considered as the onset

of non-Darcy flow regime. The following formulations of the Reynolds number are here considered:

$$Re_k = \frac{\rho U \sqrt{k_D}}{\mu} \tag{9a}$$

$$Re_l = \frac{\rho U l}{\mu} \tag{9b}$$

Values of these quantities associated with the onset of the non-Darcy regime in the analyzed Beadpack sample are listed in Table 3. As an additional example of the quality of the comparison between the results of the current study and those of Muljadi et al. [14], Fig. 5 depicts the dependence of k_{app} (Eq. 6) on Re_L.
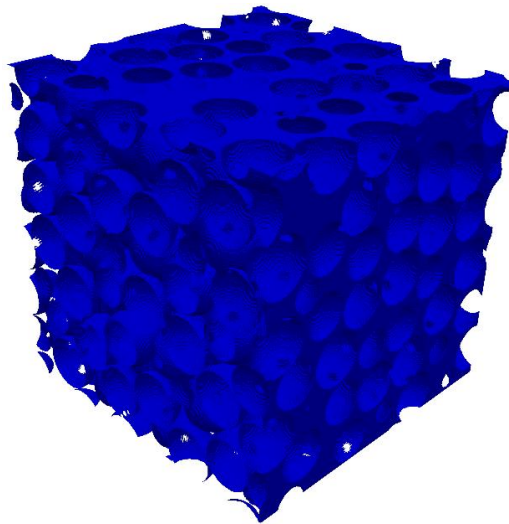
Fig. 3. Pore space geometry of the X-ray imaged Beadpack sample [14] here considered for the assessment of the numerical approach developed in our study (sample porosity is 0.359).

Table 2. Comparison of the numerical results of Muljadi et al. [13] and El-Zehairy et al. [8] and those of the present study for permeability (k_D) of the Beadpack sample depicted in Fig. 3.

Sample	Resolution (μm)	Characteristic Length (μm)	Total voxels	Porosity	$k_D \times 10^{12} (m^2)$		
					Muljadi et al. [14]	El-Zehairy et al. [8]	Present study
Beadpack	2.0	100	300^3	0.359	5.57	5.43	5.43
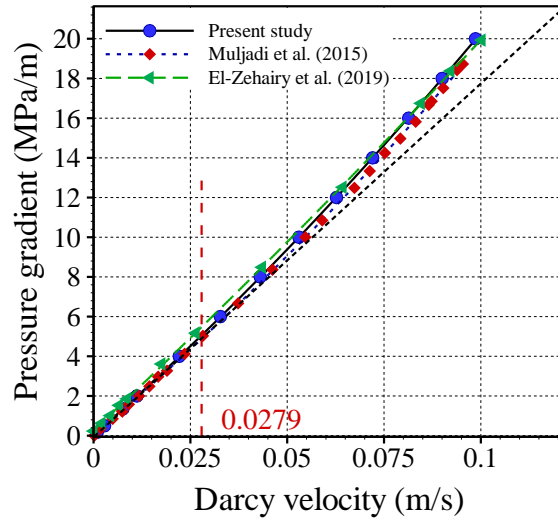
Fig. 4. Imposed pressure gradient across the X-ray imaged Beadpack sample (Fig. 3) versus the evaluated average flux (i.e., Darcy velocity) as a result of our computations and those of Muljadi et al. [14] and El-Zehairy et al. [8]. The value of Darcy velocity at which the onset of non-Darcy flow regime starts to be visible is also included, the dashed line representing linear (i.e., Darcy) behavior.

Table 3. Values of Re_k and Re_L corresponding to the onset of a non-Darcy flow regime for the Beadpack sample (Fig. 3) as obtained in this study and by Muljadi et al. [14] and El-Zehairy et al. [8].

	Reynolds number corresponding to the onset of non-Darcy flow regime	
	Re_k	Re_l
Muljadi et al. [14]	6.64×10^{-2}	2.79
El-Zehairy et al. [8]	4.15×10^{-2}	1.78
Present study	6.58×10^{-2}	2.71
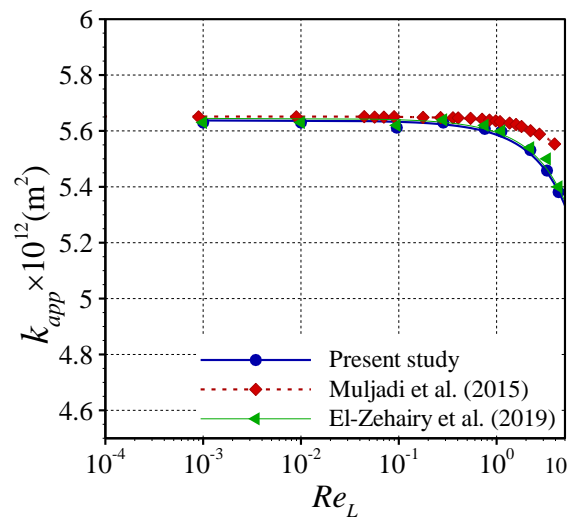
Fig. 5. Values of k_{app} versus Re_L resulting from the current study and from Muljadi et al. [14] and El-Zehairy et al. [8].

13

The impact of porosity and PPI on the pore-scale velocity field can be visually appraised in Fig. 6, which depicts (steady-state) streamlines (velocity values being presented through a color map) for samples 4 and 9 which are characterized by lowest porosity / largest PPI and largest porosity / lowest PPI values, respectively (see Table 1). Due to the high porosity of the samples, the flow field (as expressed in terms of streamlines spatial distribution) is well connected in both cases, a more tortuous flow pattern being noticeable for sample 4 that is associated with a larger PPI value and hence a more complex pore structure. It is noted that a significant increase of PPI yields a visibly enhanced complexity of the velocity distributions, which appears to be characterized by a high degree of spatial heterogeneity.

(a)   (b)
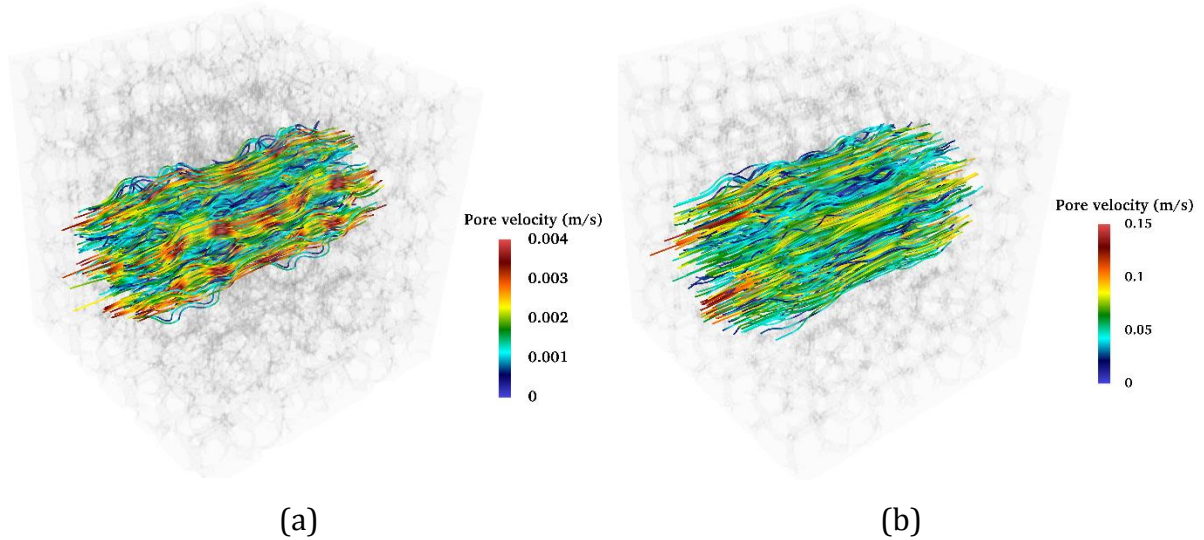
Fig. 6. Streamlines (velocity values are illustrated through a color map) for synthetic samples (a) 4 (Porosity = 0.85, PPI = 40), (b) 9 (Porosity = 0.95, PPI = 10) listed in Table 1.

Fig. 7 depicts spatial distributions of the norm of pore velocities and streamline patterns for a collection of samples under given imposed pressure gradient. For completeness, the corresponding tortuosity values are also included. As noted above, one can see that the flow field varies spatially forming wavy patterns, a higher degree of tortuosity and spatial heterogeneity of flow across samples being generally associated with increased PPI values (compare Figs. 7 a, b, and c) and differing porosities (compare Figs. 7 c and d). It is recalled that tortuosity is evaluated through the numerical pore velocity field and is defined as the ratio between the average of the magnitude of the velocity component parallel to the macroscopic flow direction ($\langle u_x \rangle$) and the spatial average of the velocity field magnitude over the pore space ($\langle u_p \rangle$) [52]:

14

$$Tortuosity = \frac{\langle u_x \rangle}{\langle u_p \rangle} \tag{10}$$

This method and formulation is also employed by [14] to evaluate tortuosity in porous structures associated with natural rocks. It is known that tortuosity is a descriptor of an average elongation of fluid streamlines in a porous medium as compared to free flow (see, e.g., [52]). While there are several methods for the evaluation of tortuosity, one can assess it on the basis the velocity field, without the need of determining streamlines. This highly simplifies the determination of tortuosity in complex geometries, including porous structures of the type here considered.

Tortuosity = 1.0596

Tortuosity = 1.0640

(a)

(b)

Tortuosity = 1.0782

Tortuosity = 1.0954

(c)

(d)
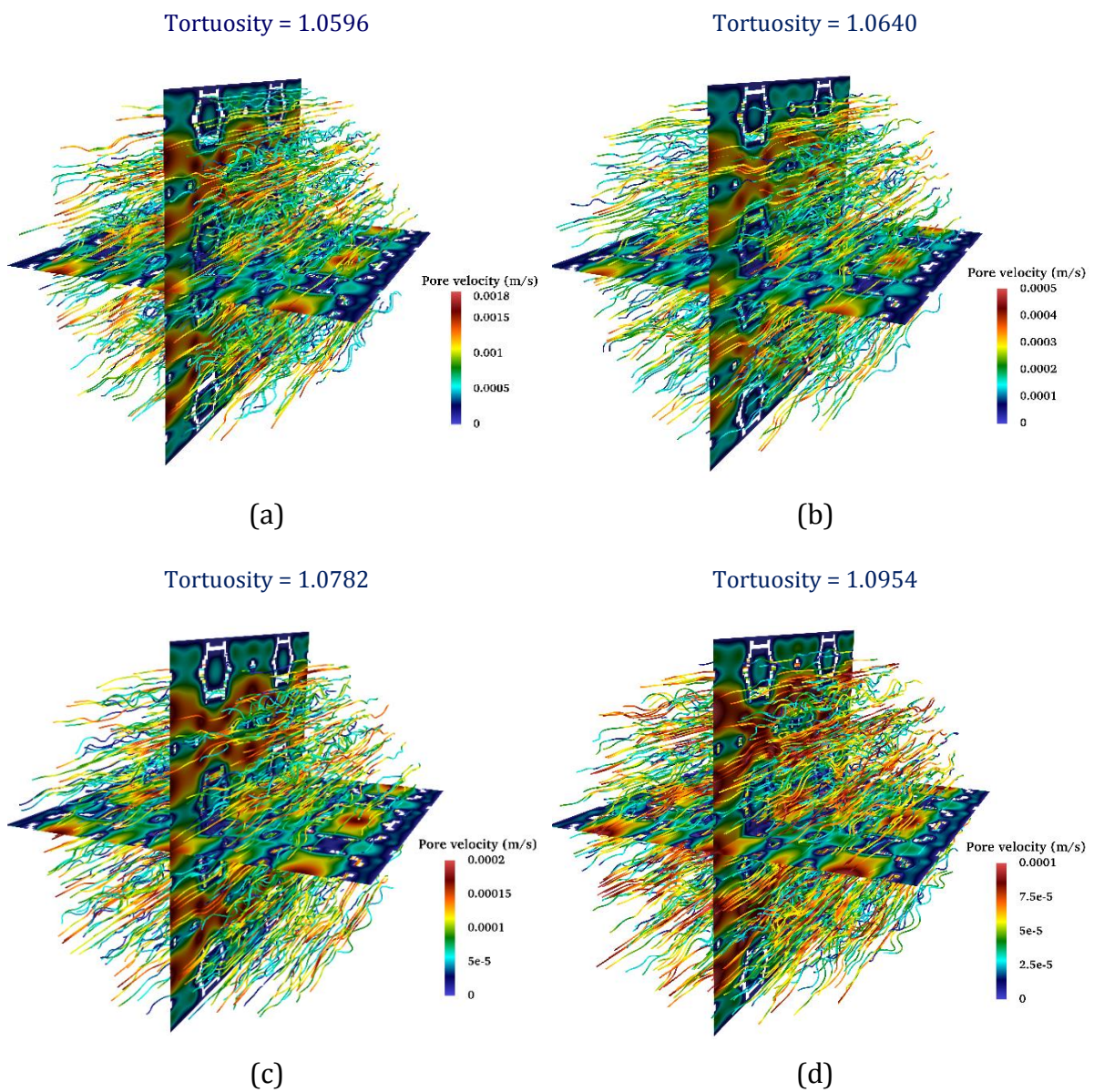
Fig. 7. Spatial distribution of the norm of pore velocities for a given imposed pressure gradient (i.e., 10 (Pa/m)) and samples (a) 9 (Porosity = 0.95; PPI = 10); (b) 10 (Porosity = 0.95; PPI = 20); (c) 11 (Porosity = 0.95, PPI = 30); and (d) 3 (Porosity = 0.85; PPI = 30).

Fig. 8 juxtaposes the dependence of k_{app} and tortuosity on Re_k for two selected samples, associated with a given porosity and diverse PPI values. These results suggest that complexity of the flow pathways (as expressed through tortuosity) increases with values of the Reynolds number for scenarios associated with (macro-scale) non-Darcy regimes.

Results of the study also reveal that pore geometry has a significant effect on the spatial organization of flow velocity and energy loss (which is in turn related to pressure loss). Decreasing porosity and increasing PPI yields an enhanced level of complexity of the flow patterns, even as velocity gradients across the simulation domains tend to decrease. A quantitative analysis of these elements is further offered in the following.
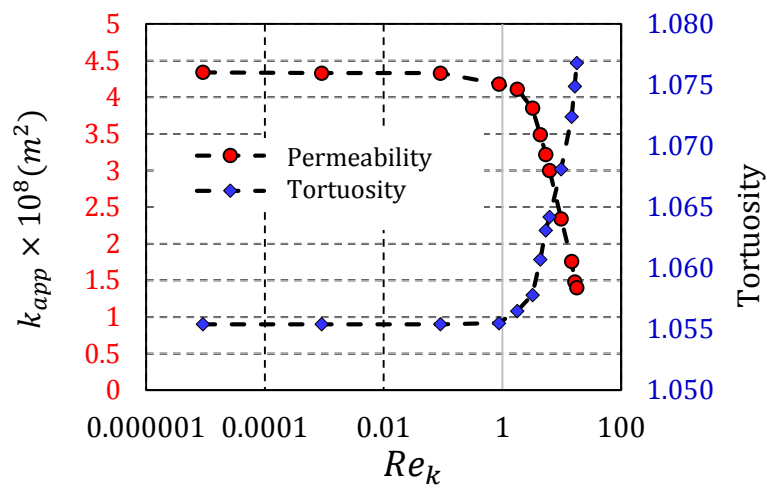

(a)
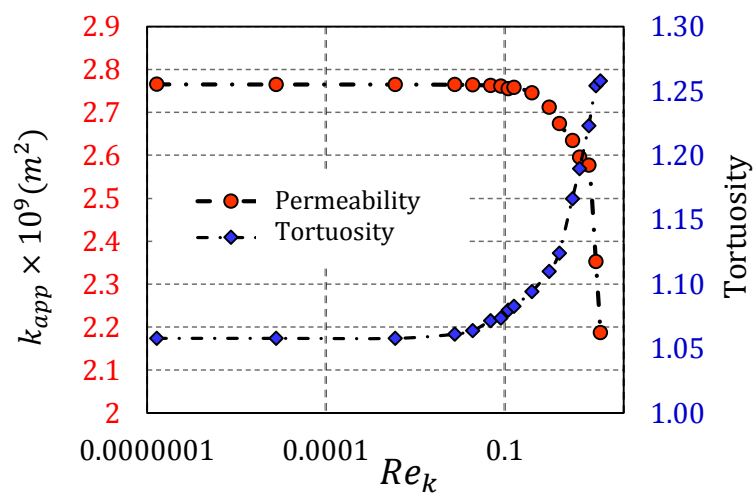
(b)

Fig. 8. Dependence of k_{app} (primary vertical axis) and tortuosity (secondary vertical axis) on Re_k for synthetic samples (a) 1 (Porosity = 0.85; PPI = 10) and (b) 2 (Porosity = 0.85; PPI = 40) of Table 1.

Fig. 9 depicts spatial distributions of pore flow velocities across samples 2, 3, and 4 (see Table 1 for a description of the samples) which are characterized by the same porosity (i.e., equal to 0.85) and differing PPI values. While increasing PPI yields pore velocity fields with reduced magnitude range (as shown by the color map in Fig. 9), it leads to an increased complexity of the structure of the pore space within which the fluid moves, as discussed above. Additionally, it is noted that an increased level of spatial variability of the pore-scale velocity field is associated with the samples with larger PPI numbers, as documented through the highest local velocity contrasts visibly appearing in Fig. 9. Therefore, the heterogeneity in the pore structure of the metal foams (here assessed in terms of PPI) appears to cause the flow to be associated with a non-Darcy regime even at low values of Reynolds number (see below and Table 5 for a quantitative analysis). This, in turn, suggests that there might be an associated enhancement of the heat transfer capability of the system ([53], [54]), which is a major feature that should be considered for efficient design of the industrial metal foams.

It should be noticed that the pore structure of these open-cell metal foams is generated using a repetitive pattern, so that the geometry structure is isotropic, this reflecting also on permeability which can then be considered as isotropic. Investigation of the flow patterns across anisotropic samples will be subject to future studies.
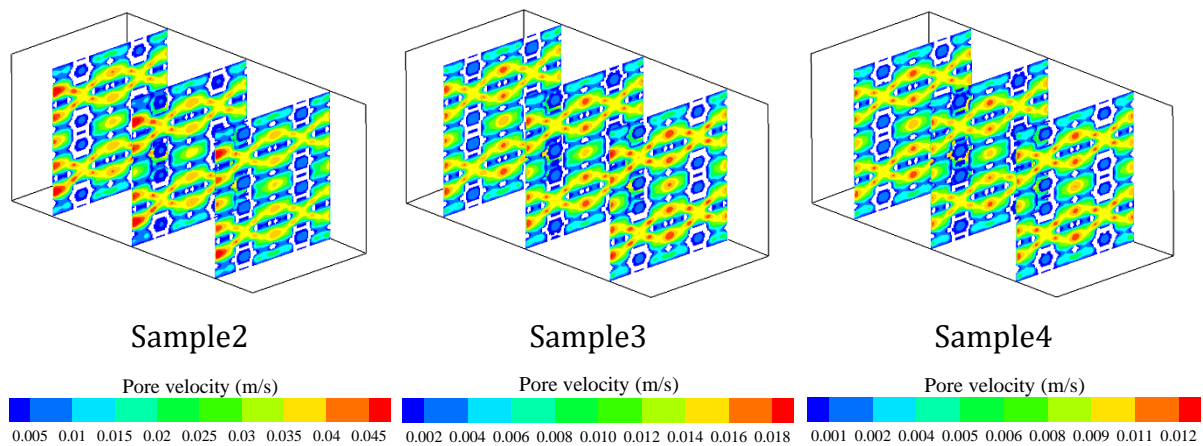
Fig. 9 Spatial distribution of pore flow velocities across samples (a) 2, (b) 3, and (c) 4 (see Table 1 for description of the samples) which are characterized by the same porosity (i.e., equal to 0.85) and differing PPI values for a fixed pressure gradient of 1 (kPa/m).
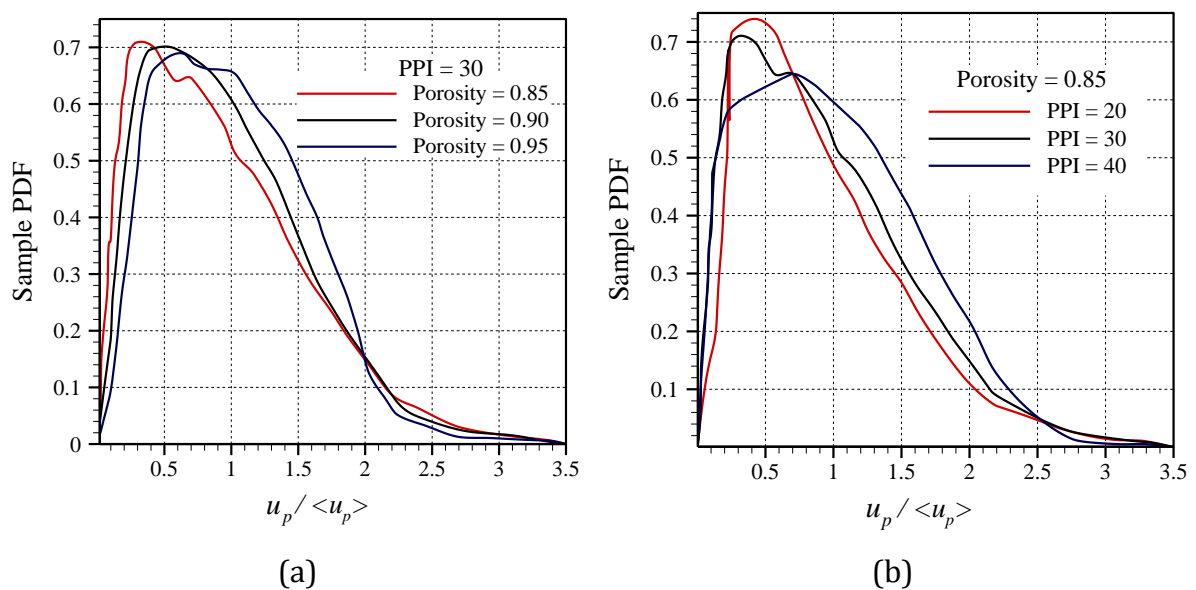
Fig. 10 depicts sample probability density functions (PDFs) of normalized Eulerian pore velocities for various combinations of porosity and PPI values. These results are complemented by Table 4 which lists values of mean velocity and coefficient of variation for the samples illustrated in Fig. 10. One can note that peak values are seen to decrease

as porosity and PPI increase and PDFs tends to be characterized by a slight increase of the coefficient of variation (see also Table 4) for the samples with more heterogenous pore scale structure (i.e., with the largest PPI). The left skewed character of the PDFs reveals that a portion of the pore space locally experiences velocities significantly different from the average pore velocity magnitude. These differences from the average velocity value are linked to the occurrence of localized regions with high pore velocity gradients (corresponding to the red spots in Fig. 9). These are the areas that may be at the core of the onset of non-Darcy flow even in the presence of low values of Reynolds number and can potentially enhance heat exchange rates. The documented local fluctuation of pore velocity is strongest for the samples with the largest PPI values. This latter observation is also consistent with results stemming from a typical analysis of the spatial correlation of the evaluated velocity fields.

Fig. 11 depicts sample variograms of pore-scale velocity evaluated across a cross section oriented along the flow direction for the metal foam samples 9, 10, 11, and 12 which are characterized by the same porosity (which is the highest amongst the samples) and differing PPI values. Fig. 11 also include results of variogram modeling, for completeness. For ease of visualization, sample variograms are normalized with respect to the sill of the corresponding interpretive model. Estimates of variogram model parameters as well as of their associated uncertainty (expressed through the ensuing estimation variance) are quantified through a classical Maximum Likelihood approach. The theoretical variogram model which best interprets the observations is selected upon relying on the Kashyap model discrimination criterion (e.g., [55],[56],[57] and references therein) that has been applied considering a Gaussian, a simple exponential, and a spherical model, which are amongst the most frequently considered interpretive models (details not shown). It is noted that the selection of the variogram model depends on the value of PPI associated with the system. For example, while Samples 9 and 12 are associated with a spherical model, a simple exponential model appears to best interpret the spatial structure of the velocity variogram across Samples 10 and 11. While of interest, given the objective of the study, we defer to future works the analysis of the way geometrical features of the system might be related to the functional format of the variogram of Eulerian pore-scale velocities across these systems.

Otherwise, these results clearly show that by increasing PPI there is an overall decrease in the variogram integral scale, which is associated with the strength of the

spatial correlation of the pore velocity data. With reference to Fig. 11, it is noted that estimates of variogram integral scale (in m) are equal to 0.0006 (estimated range of 0.0016, with associated standard deviation of 1.0×10^{-5}), 0.00027 (estimated range of 0.00027 with an associated standard deviation of 7.3×10^{-6}), 0.00019 (estimated range of 0.00019 with an associated standard deviation of 6.8×10^{-6}), and 0.00015 (estimated range of 0.00039 with an associated standard deviation of 3.4×10^{-6}) for Samples 9, 10, 11, and 12, respectively. This in turn implies an increase in the degree of spatial disorder of the pore velocity field which eventually triggers the onset of a non-Darcy regime at lower Reynolds numbers within the samples with higher PPI values.

(a)   (b)

Fig. 10. Sample probability density function of (normalized) pore flow velocities at a given pressure gradient of 1 kPa/m and corresponding to samples with (a) a given porosity and differing PPI values or (b) a given PPI and differing porosity values (here, u_p denotes the norm of pore velocity).

Table 4. Average velocity and coefficient of variation of sample pore velocity values associated with the systems depicted in Fig. 10.

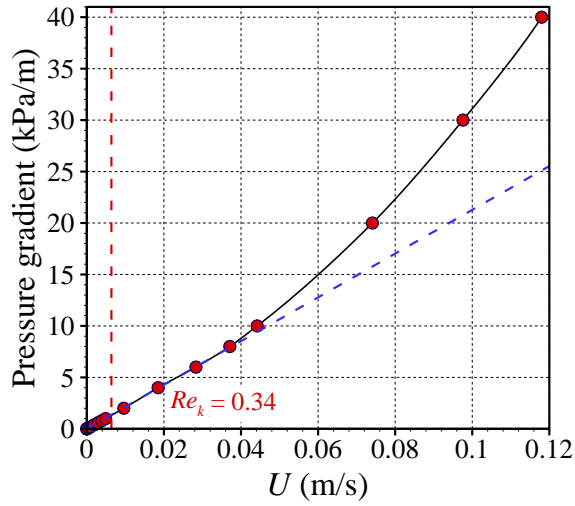| **Porosity = 0.85**			
Sample Number	PPI	Average Velocity $< u_p >$ (m/s)	Coefficient of Variation
2	20	0.123	0.053
3	30	0.048	0.057
4	40	0.031	0.059
PPI = 30			
Sample Number	Porosity	Average Velocity $< u_p >$ (m/s)	Coefficient of Variation
3	0.85	0.048	0.057
7	0.90	0.066	0.058
11	0.95	0.077	0.060
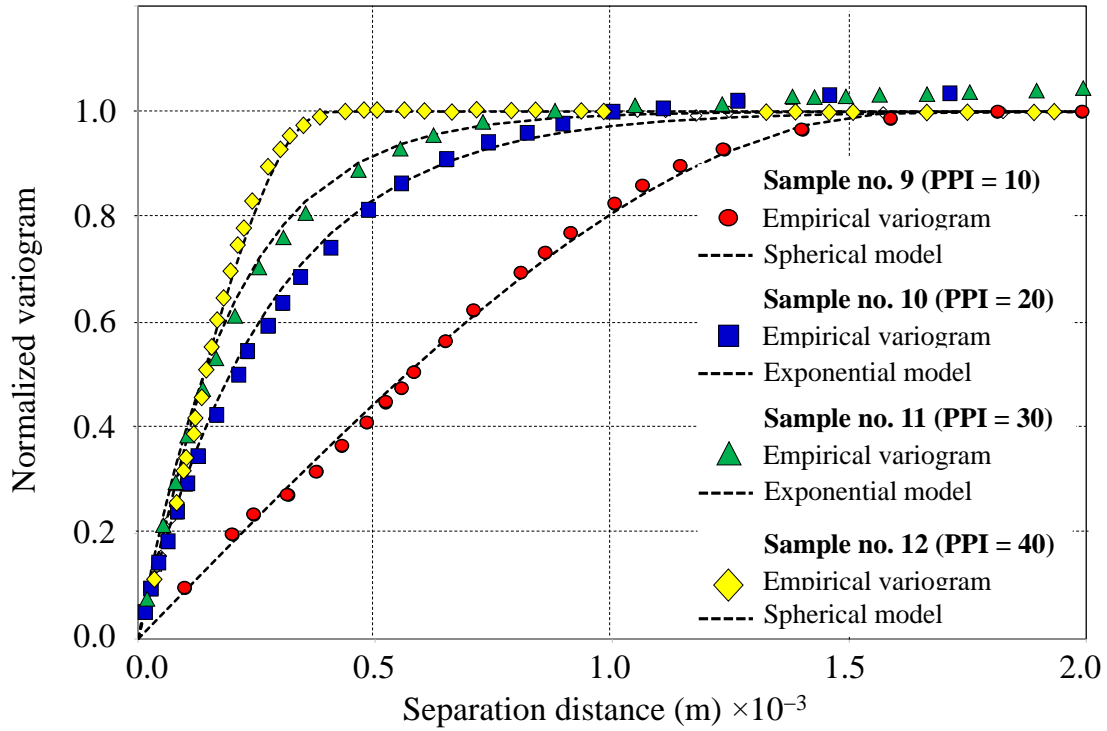
Fig. 11. Empirical variograms (symbols) of Eulerian pore velocities evaluated across a cross section oriented along the flow direction (under an imposed pressure gradient of 100 Pa/m) for the metal foam samples 9, 10, 11, and 12 which are characterized by the same porosity (= 0.95) and differing PPI values. Corresponding results from variogram modeling are also depicted (dashed curves).

Values of Reynolds number corresponding to the onset of non-linear flow behavior in some of the analyzed foam samples are listed in Table 5. These results show that the samples characterized by a porosity equal to 0.85 are linked to values of the Reynolds number at which the non-linear flow starts that decrease from 99 to 20 upon increasing PPI values from 10 to 40. Further to this, it is noted that at PPI = 10 more than 10% increase of the porosity is required to significantly reduce the critical value of the Reynolds number. This, in turn, suggests that PPI can have a stronger control on the onset of a nonlinear flow regime than porosity in the open-cell metal foams with the pore structures analyzed in this study. While in the presence of higher porosities (e.g., porosity = 0.90) the effects of PPI on the emergence of non-linear flow can be less strong, our results suggest that there might be an optimal combination of PPI and porosity values to yield desired conditions, a topic which can be subject to future analyses.

Table 5. Values of Reynolds number corresponding to the onset of non-linear flow behavior for selected synthetic foam samples.

| Sample Number	Characteristics		Onset of non-Darcy flow	
	Porosity	PPI	$Re_K < 2$	$Re_l < 100$
PPI EFFECT; Porosity = 0.85				
1	0.85	10	1.77	99
2	0.85	20	0.45	26.2
3	0.85	30	0.34	19.5
4	0.85	40	0.28	16.5
POROSITY EFFECT; PPI = 10				
1	0.85	10	1.77	99
5	0.90	10	1.58	82.5
9	0.95	10	1.44	60

Fig. 12 depicts the dependence between pressure loss and average (Darcy) pore velocity across the metal foam samples investigated. Note that the blue line depicted in the figure represents a (linear) Darcy behavior, which is mainly related to small pressure losses. Otherwise, red symbols and the black curves correspond to the behavior described by the numerical results and the Forchheimer model (see Eq. 4), respectively. It is observed that increasing PPI values favor a reduction in the value of the critical Reynolds number (which is defined as the Reynolds number at which there is the emergence of a non-Darcy regime). This is in line with the previously observed increased complexity of the pore space structure, and, ultimately, tortuosity. These findings are also consistent with prior studies on metal foam samples [58] and further support the observation that in metal foams a Darcy model holds only across a limited range of the average fluid velocity and only in the presence of low pressure gradients (this is clearly seen in Fig. 12, where pressure gradients at which flow behaves linearly are typically less than 3 kPa/m). Thus, a Forchheimer model (of the kind embedded in Eq. 4) should be applied to analyze flow behavior in metal foams operating under typical conditions which are considered in industrial applications to enhance heat and mass exchange rates (see also [59]).
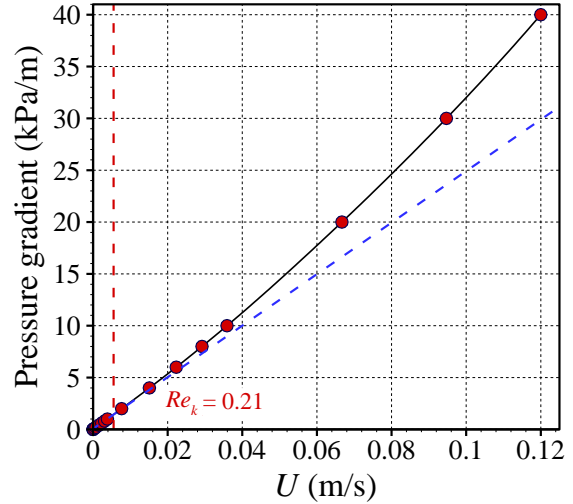
Sample 3 (Porosity = 0.85, PPI = 30)
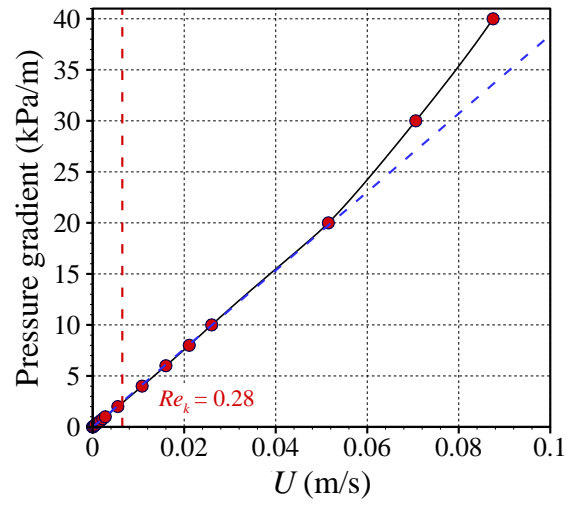
Sample 4 (Porosity = 0.85, PPI = 40)
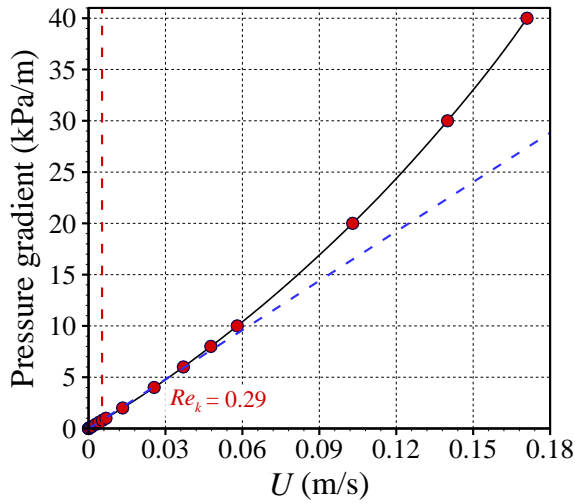
Sample 11 (Porosity = 0.95, PPI = 30)

Sample 12 (Porosity = 0.95, PPI = 40)

Fig. 12. Pressure gradient versus velocity for samples with different PPI and porosity values. The onset of the non-Darcy flow regime (as expressed in terms of Re_k) is displayed by the vertical red dashed lines. The blue line represents a (linear) Darcy behavior; red symbols and the black curves correspond to the behavior described by the numerical results and the Forchheimer model (see Eq. 4), respectively.

Fig. 13 depicts apparent permeability k_{app} versus Re_k for all samples analyzed. These results are complemented by Table 6, where the resulting intrinsic permeability, Forchheimer permeability, and the Forchheimer coefficient (β) are listed. The value of β is assessed through the slope of the curves describing $\frac{1}{k_{app}}$ versus $\frac{\rho U}{\mu}$ (see Eq. 7) within the Forchheimer regime. These results reveal that, for a given porosity, apparent permeability decreases with increasing PPI. In samples with porosity equal to 0.85, apparent permeability decreases approximately 10 times upon increasing PPI from 10 to 40.

22
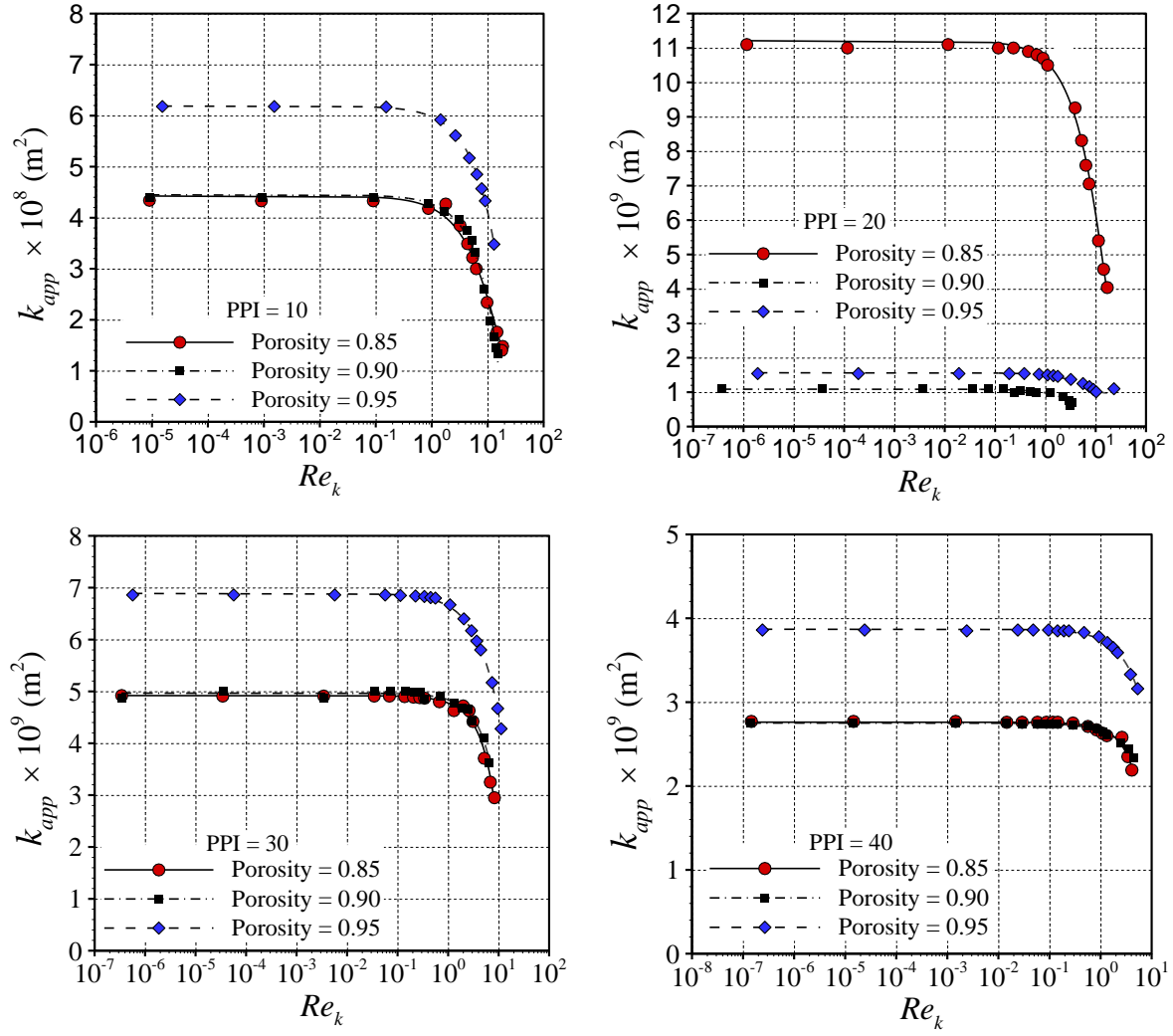
Fig. 13. Values of k_{app} versus Re_k for all synthetic samples listed in Table 1.

Table 6. Values of Darcy and non-Darcy permeabilities and of coefficient β (see Eq. 7) for all synthetic samples.

| Sample number	Porosity	PPI	$k_D \times 10^8 (m^2)$	$k_F \times 10^8 (m^2)$	$\beta \times 10^{-4}(m^{-1})$
1	0.85	10	4.347	4.271	8.63
2	0.85	20	1.119	1.032	17.03
3	0.85	30	0.488	0.421	25.60
4	0.85	40	0.271	0.214	34.22
5	0.90	10	4.409	4.288	7.98
6	0.90	20	1.140	1.062	14.09
7	0.90	30	0.492	0.458	23.90
8	0.90	40	0.275	0.251	31.91
9	0.95	10	6.195	5.823	6.247
10	0.95	20	1.546	1.372	12.43
11	0.95	30	0.686	0.588	18.74
12	0.95	40	0.386	0.291	24.81

Fig. 14 reveals that k^* (see Eq. 8) is virtually insensitive to Re_k across the region characterized by the Darcy regime, where values of apparent and intrinsic permeability coincide. Otherwise, k^* decreases with increasing Reynolds number within the non-Darcy flow regime region, consistent with an associated decrease of apparent permeability.
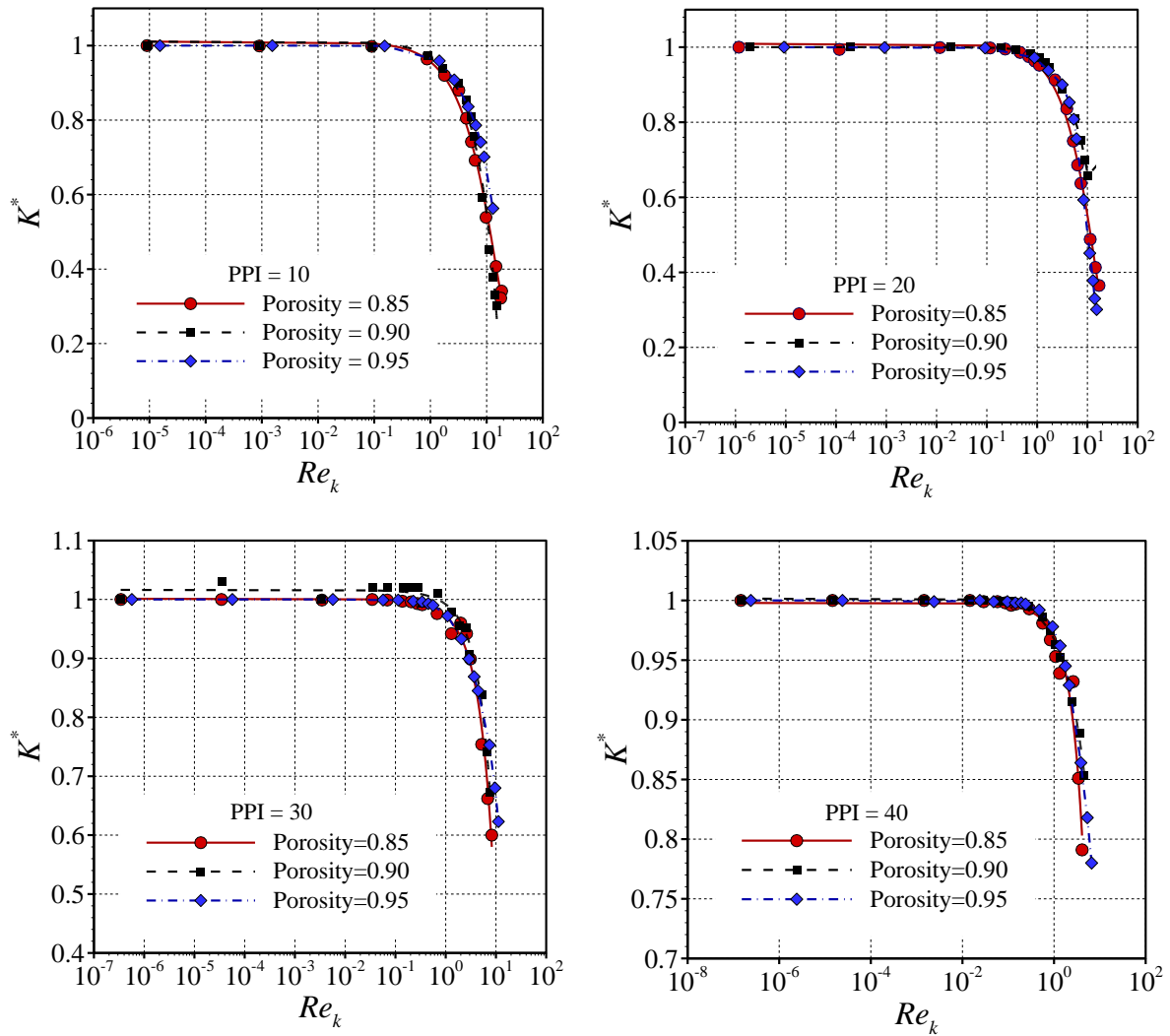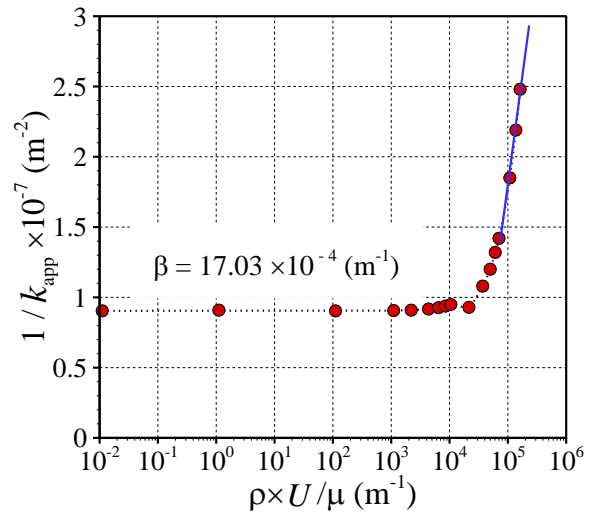

Fig. 14. Dimensionless permeability k^* (Eq. 8) versus Re_k for the synthetic samples analyzed.

Fig. 15 complements these results by depicting $\frac{1}{k_{app}}$ versus $\frac{\rho U}{\mu}$. Considering the results encapsulated in Fig. 15 and Table 7, it is noted that the highest values of β correspond to the samples with the largest PPI values, providing further support to the importance of including the impact of the Forchheimer inertial term in modeling flow across these types of highly porous and heterogeneous systems.
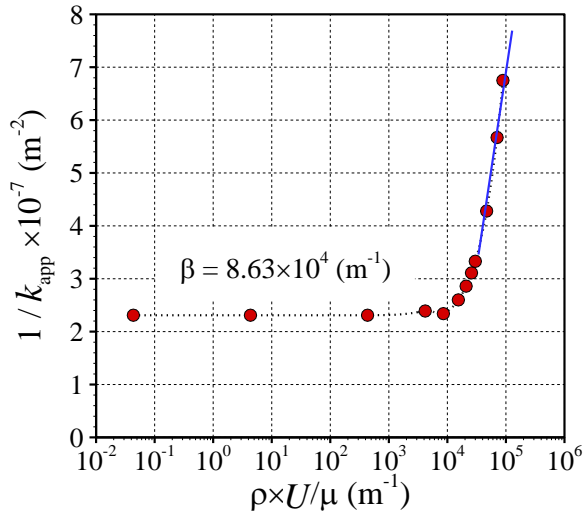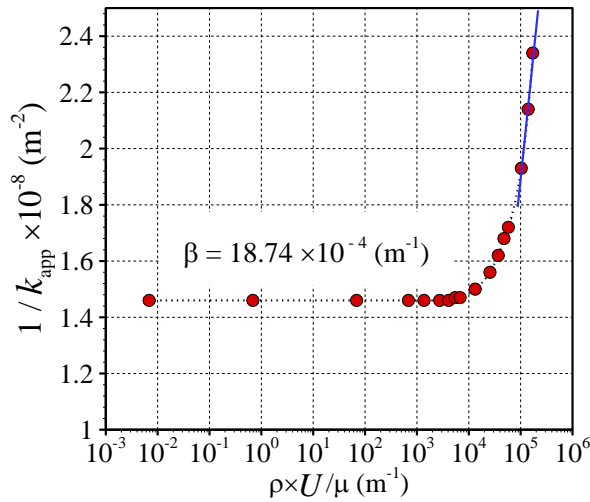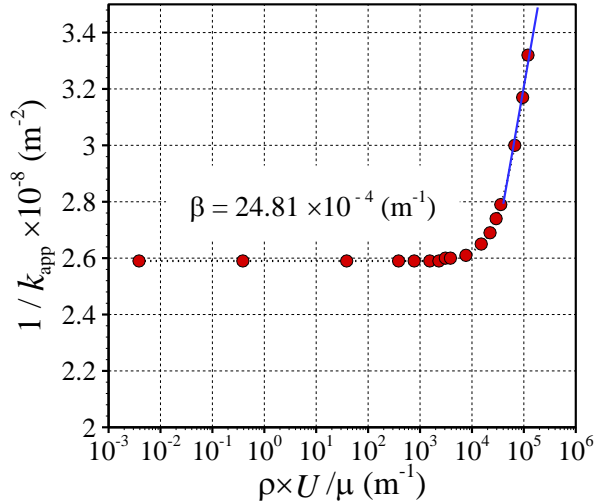
Sample 1 (Porosity = 0.85, PPI = 10)   Sample 2 (Porosity = 0.85, PPI = 20)

Sample 11 (Porosity = 0.95, PPI = 30)   Sample 12 (Porosity = 0.95, PPI = 40)

Fig. 15. Values of $1/k_{app}$ versus $(\frac{\rho U}{\mu})$ for four selected samples with differing PPI and porosity values.

4. Conclusions

Results of a suite of detailed high-resolution pore-scale direct numerical simulations are presented to investigate key aspects of the onset of (macro-scale) non-Darcy flow regimes through open-cell metal foams with differing geometrical attributes. The study rests on synthetically generated pore structures, computational analyses of pore-scale velocity fields being performed to explore the effect of porosity and number of pores per inch (PPI) of the foam structures on (*i*) the emergence of non-Darcy flow, (*ii*) permeability associated with Darcy and non-Darcy regimes, and (*iii*) Forchheimer

coefficient as well as apparent permeability. The study leads to the following major conclusions.

1) Pore geometry in such highly porous materials markedly affects the spatial organization of flow velocity. Decreasing porosity and increasing PPI favors an enhanced level of complexity of the flow patterns. The degree of heterogeneity in the pore space structure of the metal foams (as expressed in terms of PPI) is seen to promote the occurrence of a non-Darcy regime even at low values of Reynolds number, this finding being potentially relevant to assist enhancement of heat transfer capability of foams.

2) Local fluctuations of pore-scale velocities are seen to be highest for the samples with the largest PPI values. This observation is also consistent with results stemming from a characterization of the spatial correlation structure of the evaluated Eulerian velocity fields where we document an increase in the degree of spatial disorder of the pore velocity field. The latter is intimately related to the observed decrease of the spatial integral scale of velocities, which is at the basis of the onset of a non-Darcy regime for values of the Reynolds number that tends to decrease with increasing PPI values. On these bases, it is shown that flow in the open-cell metal foams analyzed is predominantly in a non-Darcy regime

3) The number of pores per inch is seen to exert a stronger control on the onset of a nonlinear flow regime than porosity across the systems we analyze. For example, at PPI = 10 more than 10% increase of the porosity is required to significantly reduce the value of the Reynolds number at which no-Darcy effects are visible. Overall, our results suggest that there might be an optimal combination of PPI and porosity values that might be suitable to achieve desired strength of non-linear effects, a topic which can be subject to future analyses.

4) For a given porosity, apparent permeability decreases with increasing PPI. Our results suggest that the highest values of the Forchheimer coefficient are associated with the samples with the largest PPI values. All these elements support the importance of including the impact of inertial terms in modeling flow across these types of highly porous and heterogeneous systems.

Upon leveraging on the results of the present study, future developments aim at investigating the effect of non-linear flow behavior on heat transfer across open-cell metal foam samples with various degrees of geometrical complexities to contribute to

applications in sustainable energy practices. Future extensions of the study will also include detailed analyses of flow and solute transport processes, including various types of chemical reactions which can be of interest in the context of environmental engineering applications.

DATA AVAILABILITY

Data supporting the findings of this study are available from the corresponding author upon reasonable request.

REFERENCES

[1] T. Fang, Y. Zhang, B. Ding, Y. Yan, and J. Zhang, 'Static and dynamic behavior of CO2 enhanced oil recovery in nanoslits: Effects of mineral type and oil components', *Int. J. Heat Mass Transf.*, vol. 153, p. 119583, Jun. 2020, doi: 10.1016/j.ijheatmasstransfer.2020.119583.

[2] F. Selimefendigil and H. F. Öztop, 'Effects of local curvature and magnetic field on forced convection in a layered partly porous channel with area expansion', *Int. J. Mech. Sci.*, vol. 179, p. 105696, Aug. 2020, doi: 10.1016/j.ijmecsci.2020.105696.

[3] A. J. Chamkha, F. Selimefendigil, and H. F. Oztop, 'Effects of a Rotating Cone on the Mixed Convection in a Double Lid-Driven 3D Porous Trapezoidal Nanofluid Filled Cavity under the Impact of Magnetic Field', *Nanomaterials*, vol. 10, no. 3, Mar. 2020, doi: 10.3390/nano10030449.

[4] E. Baioni, M. Mousavi Nezhad, G. M. Porta, and A. Guadagnini, 'Modeling solute transport and mixing in heterogeneous porous media under turbulent flow conditions', *Phys. Fluids*, vol. 33, no. 10, p. 106604, 2021. https://doi.org/10.1063/5.0065734.

[5] M. Mousavi Nezhad, M. Rezania, and E. Baioni, 'Transport in Porous Media with Nonlinear Flow Condition', *Transp. Porous Media*, vol. 126, no. 1, pp. 5–22, Jan. 2019, doi: 10.1007/s11242-018-1173-4.

[6] D. Zhang, S. Li, and Y. Li, 'Numerical investigation on acidic hydrothermal reactive flow in fractured rocks using a modified LBM model', *Sustain. Energy Technol. Assess.*, vol. 48, p. 101585, Dec. 2021, doi: 10.1016/j.seta.2021.101585.

[7] Q. Xiong, T. G. Baychev, and A. P. Jivkov, 'Review of pore network modelling of porous media: experimental characterisations, network constructions and applications to reactive transport', *J. Contam. Hydrol.*, vol. 192, pp. 101–117, 2016. https://doi.org/10.1016/j.jconhyd.2016.07.002.

[8] A. A. El-Zehairy, M. M. Nezhad, V. Joekar-Niasar, I. Guymer, N. Kourra, and M. A. Williams, 'Pore-network modelling of non-Darcy flow through heterogeneous porous media', *Adv. Water Resour.*, vol. 131, p. 103378, 2019. https://doi.org/10.1016/j.advwatres.2019.103378.

[9] E. Baioni, G. M. Porta, M. M. Nezhad, and A. Guadagnini, 'Assessment of turbulence effects on effective solute diffusivity close to a sediment-free fluid interface', *Stoch. Environ. Res. Risk Assess.*, vol. 34, no. 12, pp. 2211–2228, 2020. https://doi.org/10.1007/s00477-020-01877-y.

[10] M. J. Blunt *et al.*, 'Pore-scale imaging and modelling', *Adv. Water Resour.*, vol. 51, pp. 197–216, 2013. https://doi.org/10.1016/j.advwatres.2012.03.003.

[11] A. Grillo, M. Carfagna, and S. Federico, 'Non-Darcian flow in fibre-reinforced biological tissues', *Meccanica*, vol. 52, no. 14, pp. 3299–3320, 2017. https://doi.org/10.1007/s11012-017-0679-0.

[12] B. Bijeljic, A. Raeini, P. Mostaghimi, and M. J. Blunt, 'Predictions of non-Fickian solute transport in different classes of porous media using direct simulation on pore-scale images', *Phys. Rev. E*, vol. 87, no. 1, p. 013011, 2013. https://doi.org/10.1103/PhysRevE.87.013011.

[13] B. Bijeljic, P. Mostaghimi, and M. J. Blunt, 'Insights into non-Fickian solute transport in carbonates', *Water Resour. Res.*, vol. 49, no. 5, pp. 2714–2728, 2013. https://doi.org/10.1002/wrcr.20238.

[14] B. P. Muljadi, M. J. Blunt, A. Q. Raeini, and B. Bijeljic, 'The impact of porous media heterogeneity on non-Darcy flow behaviour from pore-scale simulation', *Adv. Water Resour.*, vol. 95, pp. 329–340, 2016. https://doi.org/10.1016/j.advwatres.2015.05.019.

[15] M. Mousavi Nezhad, A. A. Javadi, and F. Abbasi, 'Stochastic finite element modelling of water flow in variably saturated heterogeneous soils', *Int. J. Numer. Anal. Methods Geomech.*, vol. 35, no. 12, pp. 1389–1408, 2011. https://doi.org/10.1002/nag.966.

[16] M. Mousavi Nezhad, 'Stochastic finite element modelling of flow and solute transport in dual domain system', International Journal for Numerical and Analytical Methods in Geomechanics 35(12):1389 - 1408 August 2011. DOI:10.1002/nag.966.

[17] X. Guo and X. Wang, 'The impact of flow displacement patterns on hydraulic tortuosity for unsaturated flow', *Phys. Fluids*, vol. 33, no. 2, p. 023308, 2021. https://doi.org/10.1063/5.0037816.

[18] A. Banerjee, S. Pasupuleti, K. Mondal, and M. M. Nezhad, 'Application of data driven machine learning approach for modelling of non-linear filtration through granular porous media', *Int. J. Heat Mass Transf.*, vol. 179, p. 121650, 2021. https://doi.org/10.1016/j.ijheatmasstransfer.2021.121650.

[19] C. Gadd, W. Xing, M. M. Nezhad, and A. A. Shah, 'A surrogate modelling approach based on nonlinear dimension reduction for uncertainty quantification in groundwater flow models', *Transp. Porous Media*, vol. 126, no. 1, pp. 39–77, 2019. https://doi.org/10.1007/s11242-018-1065-7.

[20] F. Selimefendigil and H. F. Öztop, 'Magnetohydrodynamics forced convection of nanofluid in multi-layered U-shaped vented cavity with a porous region considering wall corrugation effects', *Int. Commun. Heat Mass Transf.*, vol. 113, p. 104551, Apr. 2020, doi: 10.1016/j.icheatmasstransfer.2020.104551.

[21] A. J. Chamkha and F. Selimefendigil, 'MHD Free Convection and Entropy Generation in a Corrugated Cavity Filled with a Porous Medium Saturated with Nanofluids', *Entropy*, vol. 20, no. 11, Nov. 2018, doi: 10.3390/e20110846.

[22] A. J. Chamkha, F. Selimefendigil, and M. A. Ismael, 'Mixed convection in a partially layered porous cavity with an inner rotating cylinder', *Numer. Heat Transf. Part Appl.*, vol. 69, no. 6, pp. 659–675, Mar. 2016, doi: 10.1080/10407782.2015.1081027.

[23] R. S. Ferfera and B. Madani, 'Thermal characterization of a heat exchanger equipped with a combined material of phase change material and metallic foams', *Int. J. Heat Mass Transf.*, vol. 148, p. 119162, Feb. 2020, doi: 10.1016/j.ijheatmasstransfer.2019.119162.

[24] T.-T. Nguyen and K. Fushinobu, 'Effect of operating conditions and geometric structure on the gas crossover in PEM fuel cell', *Sustain. Energy Technol. Assess.*, vol. 37, p. 100584, Feb. 2020, doi: 10.1016/j.seta.2019.100584.

[25] H. Xu, L. Gong, S. Huang, and M. Xu, 'Non-equilibrium heat transfer in metal-foam solar collector with no-slip boundary condition', *Int. J. Heat Mass Transf.*, vol. 76, pp. 357–365, Sep. 2014, doi: 10.1016/j.ijheatmasstransfer.2014.04.034.

[26] S. Jain, K. R. Kumar, and D. Rakshit, 'Heat transfer augmentation in single and multiple (cascade) phase change materials based thermal energy storage: Research progress, challenges, and recommendations', *Sustain. Energy Technol. Assess.*, vol. 48, p. 101633, Dec. 2021, doi: 10.1016/j.seta.2021.101633.

[27] F. Topin, J.-P. Bonnet, B. Madani, and L. Tadrist, 'Experimental analysis of multiphase flow in metallic foam: flow laws, heat transfer and convective boiling', *Adv. Eng. Mater.*, vol. 8, no. 9, pp. 890–899, 2006. https://doi.org/10.1002/adem.200600102.

[28] A. Nokhosteen and S. Sobhansarbandi, 'Utilizing lattice Boltzmann method for heat transfer analysis in solar thermal systems: A review', *Sustain. Energy Technol. Assess.*, vol. 46, p. 101264, Aug. 2021, doi: 10.1016/j.seta.2021.101264.

[29] S. Du, Z.-X. Tong, H.-H. Zhang, and Y.-L. He, 'Tomography-based determination of Nusselt number correlation for the porous volumetric solar receiver with different geometrical parameters', *Renew. Energy*, vol. 135, pp. 711–718, 2019. https://doi.org/10.1016/j.renene.2018.12.001.

[30] A. Bhattacharya, V. V. Calmidi, and R. L. Mahajan, 'Thermophysical properties of high porosity metal foams', *Int. J. Heat Mass Transf.*, vol. 45, no. 5, pp. 1017–1031, 2002. https://doi.org/10.1016/S0017-9310(01)00220-4.

[31] V. Joshi and M. K. Rathod, 'Thermal performance augmentation of metal foam infused phase change material using a partial filling strategy: An evaluation for fill height ratio and porosity', *Appl. Energy*, vol. 253, p. 113621, 2019. https://doi.org/10.1016/j.apenergy.2019.113621.

[32] V. Chandra, S. Das, E. Peters, and J. A. M. Kuipers, 'Direct numerical simulation of hydrodynamic dispersion in open-cell solid foams', *Chem. Eng. J.*, vol. 358, pp. 1305–1323, 2019. https://doi.org/10.1016/j.cej.2018.10.017.

[33] S. Mao, N. Love, A. Leanos, and G. Rodriguez-Melo, 'Correlation studies of hydrodynamics and heat transfer in metal foam heat exchangers', *Appl. Therm. Eng.*, vol. 71, no. 1, pp. 104–118, 2014. https://doi.org/10.1016/j.applthermaleng.2014.06.035.

[34] C. Xu, Y. Mao, and Z. Hu, 'Numerical study of pore-scale flow and noise of an open cell metal foam', *Aerosp. Sci. Technol.*, vol. 82, pp. 185–198, 2018. https://doi.org/10.1016/j.ast.2018.09.002.

[35] T. Xiao, X. Yang, K. Hooman, and T. J. Lu, 'Analytical fractal models for permeability and conductivity of open-cell metallic foams', *Int. J. Heat Mass Transf.*, vol. 177, p. 121509, 2021. https://doi.org/10.1016/j.ijheatmasstransfer.2021.121509.

[36] X. Yang, T. J. Lu, and T. Kim, 'An analytical model for permeability of isotropic porous media', *Phys. Lett. A*, vol. 378, no. 30–31, pp. 2308–2311, 2014. https://doi.org/10.1016/j.physleta.2014.06.002.

[37] M. Zafari, M. Panjepour, M. D. Emami, and M. Meratian, 'Microtomography-based numerical simulation of fluid flow and heat transfer in open cell metal foams', *Appl. Therm. Eng.*, vol. 80, pp. 347–354, 2015. https://doi.org/10.1016/j.applthermaleng.2015.01.045.

[38] P. Poureslami, M. Siavashi, H. Moghimi, and M. Hosseini, 'Pore-scale convection-conduction heat transfer and fluid flow in open-cell metal foams: A three-

dimensional multiple-relaxation time lattice Boltzmann (MRT-LBM) solution', *Int. Commun. Heat Mass Transf.*, vol. 126, p. 105465, 2021. https://doi.org/10.1016/j.icheatmasstransfer.2021.105465.

[39] 'OpenFOAM® - Official home of The Open Source Computational Fluid Dynamics (CFD) Toolbox'. https://www.openfoam.com/ (accessed Dec. 20, 2020).

[40] N. Dukhan, 'Correlations for the pressure drop for flow through metal foam', *Exp. Fluids*, vol. 41, no. 4, pp. 665–672, 2006. https://doi.org/10.1007/s00348-006-0194-x.

[41] S. Y. Kim, J. W. Paek, and B. H. Kang, 'Flow and heat transfer correlations for porous fin in a plate-fin heat exchanger', *J Heat Transf.*, vol. 122, no. 3, pp. 572–578, 2000. https://doi.org/10.1115/1.1287170.

[42] S. Mancin, C. Zilio, A. Cavallini, and L. Rossetto, 'Pressure drop during air flow in aluminum foams', *Int. J. Heat Mass Transf.*, vol. 53, no. 15–16, pp. 3121–3130, 2010. https://doi.org/10.1016/j.ijheatmasstransfer.2010.03.015.

[43] S. Y. Kim, B. H. Kang, and J.-H. Kim, 'Forced convection from aluminum foam materials in an asymmetrically heated channel', *Int. J. Heat Mass Transf.*, vol. 44, no. 7, pp. 1451–1454, 2001.

[44] S. Mancin, C. Zilio, A. Diani, and L. Rossetto, 'Experimental air heat transfer and pressure drop through copper foams', *Exp. Therm. Fluid Sci.*, vol. 36, pp. 224–232, 2012. https://doi.org/10.1016/j.expthermflusci.2011.09.016.

[45] 'The Surface Evolver: Experimental Mathematics: Vol 1, No 2'. https://www.tandfonline.com/doi/abs/10.1080/10586458.1992.10504253 (accessed Dec. 13, 2020).

[46] K. Boomsma, D. Poulikakos, and Y. Ventikos, 'Simulations of flow through open cell metal foams using an idealized periodic cell structure', *Int. J. Heat Fluid Flow*, vol. 24, no. 6, pp. 825–834, 2003. https://doi.org/10.1016/j.ijheatfluidflow.2003.08.002.

[47] X. Yang, S. Feng, Q. Zhang, Y. Chai, L. Jin, and T. J. Lu, 'The role of porous metal foam on the unidirectional solidification of saturating fluid for cold storage', *Appl. Energy*, vol. 194, pp. 508–521, 2017. https://doi.org/10.1016/j.apenergy.2016.09.050.

[48] X. Yang, Y. Li, L. Zhang, L. Jin, W. Hu, and T. Jian Lu, 'Thermal and fluid transport in micro-open-cell metal foams: Effect of node size', *J. Heat Transf.*, vol. 140, no. 1, 2018. https://doi.org/10.1115/1.4037394.

[49] B. Buffel, F. Desplentere, K. Bracke, and I. Verpoest, 'Modelling open cell-foams based on the Weaire–Phelan unit cell with a minimal surface energy approach', *Int. J. Solids Struct.*, vol. 51, no. 19–20, pp. 3461–3470, 2014. https://doi.org/10.1016/j.ijsolstr.2014.06.017.

[50] S. Cunsolo, M. Iasiello, M. Oliviero, N. Bianco, W. K. Chiu, and V. Naso, 'Lord Kelvin and Weaire–Phelan foam models: Heat transfer and pressure drop', *J. Heat Transf.*, vol. 138, no. 2, 2016. https://doi.org/10.1115/1.4031700.

[51] P. Forchheimer, 'Wasserbewegung durch boden', *Z Ver Dtsch. Ing*, vol. 45, pp. 1782–1788, 1901.

[52] A. Duda, Z. Koza, and M. Matyka, 'Hydraulic tortuosity in arbitrary porous media flow', *Phys. Rev. E*, vol. 84, no. 3, p. 036319, 2011. https://doi.org/10.1103/PhysRevE.84.036319.

[53] H. Wang, L. Guo, and K. Chen, 'Theoretical and experimental advances on heat transfer and flow characteristics of metal foams', *Sci. China Technol. Sci.*, vol. 63, no. 5, pp. 705–718, May 2020, doi: 10.1007/s11431-019-1455-0.

[54] M. Sun *et al.*, 'Pore-scale simulation of forced convection heat transfer under turbulent conditions in open-cell metal foam', *Chem. Eng. J.*, vol. 389, p. 124427, 2020. https://doi.org/10.1016/j.cej.2020.124427.

[55] R. L. Kashyap, 'Optimal choice of AR and MA parts in autoregressive moving average models', *IEEE Trans. Pattern Anal. Mach. Intell.*, no. 2, pp. 99–104, 1982. doi:10.1109/TPAMI.1982.4767213.

[56] M. Riva, M. Panzeri, A. Guadagnini, and S. P. Neuman, 'Role of model selection criteria in geostatistical inverse estimation of statistical data-and model-parameters', *Water Resour. Res.*, vol. 47, no. 7, 2011. https://doi.org/10.1029/2011WR010480.

[57] A. Molinari, L. Guadagnini, M. Marcaccio, and A. Guadagnini, 'Geostatistical multimodel approach for the assessment of the spatial distribution of natural background concentrations in large-scale groundwater bodies', *Water Res.*, vol. 149, pp. 522–532, 2019. https://doi.org/10.1016/j.watres.2018.09.049.

[58] Z. Nie, Y. Lin, and Q. Tong, 'Numerical simulations of two-phase flow in open-cell metal foams with application to aero-engine separators', *Int. J. Heat Mass Transf.*, vol. 127, pp. 917–932, 2018. https://doi.org/10.1016/j.ijheatmasstransfer.2018.08.056

[59] J.-J. Hwang, G.-J. Hwang, R.-H. Yeh, and C.-H. Chao, 'Measurement of interstitial convective heat transfer and frictional drag for flow across metal foams', *J Heat Transf.*, vol. 124, no. 1, pp. 120–129, 2002. https://doi.org/10.1115/1.1416690.

APPENDIX A

The OpenFOAM software (version 7) is used in the present study to perform pore-scale flow simulations and visualization for the analyzed open-cell metal foam samples. It is recalled that OpenFOAM is a well-known open-source CFD software based on C++ programming language, which is developed for applications in science and engineering. The computational suite has been selected as it enables one to employ various solvers to simulate, visualize, and analyze complex fluid flows involving chemical reactions, turbulence, and heat transfer. Flow simulations in this study are performed using module "SimpleFoam" on OpenFOAM platform. This library provides the computational model solves system of Navier-Stokes equations for laminar incompressible fluid flow.

APPENDIX B
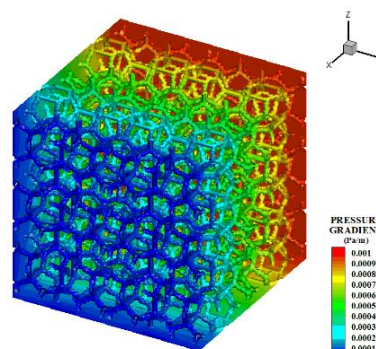
Figure 16. Computational results of the norm of the pressure gradient field associated with sample 6 of Table 1 (Porosity = 0.90 and PPI = 20).

Numerical simulations with differing mesh sizes are performed to find the optimum mesh size for each of the samples. Details about the optimum finite cell numbers and the associated values for the permeability of the samples are listed in Table 7. For simplicity, only permeabilities evaluated by the three final meshes at which convergence of the result is obtained are listed. Additionally, as an example, Fig. 16 depicts the permeability k_D values associated with the simulations related to sample 2 (which is characterized by the most complex geometry) versus the number of cells employed in the numerical analyses. These results enable us to identify Mesh #2 as appropriate for our analyses. For these simulations we relied on a workstation with 2 Intel® Xeon® CPUs (each including 16 threads @ 3.3 GHz) and 64 GB computational memory.

Table 7. Darcy permeability k_D evaluated for selected samples and corresponding to the three final meshes at which convergence of the result is obtained.

Sample number	Mesh#1 (Cell number)	Permeability $k_D \times 10^8$	Mesh#2 (Cell number)	Permeability $k_D \times 10^8$	Mesh#3 (Cell number)	Permeability $k_D \times 10^8$
1	100^3	4.543	150^3	4.416	200^3	4.346
2	100^3	1.285	150^3	1.176	200^3	1.115
3	100^3	0.490	150^3	0.495	200^3	0.492
4	100^3	0.294	150^3	0.282	200^3	0.277
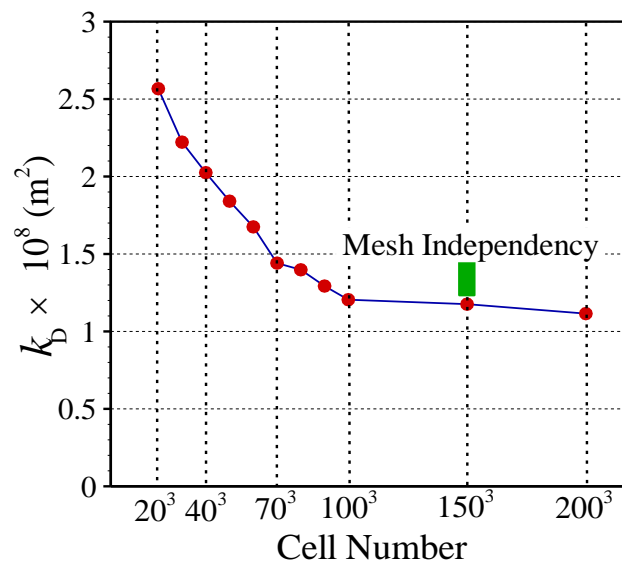
Fig. 17. Values of k_D versus the number of cells employed in the numerical analyses for sample 2.

Author statement

Hamid Moghimi: Methodology, software, solver development, validation, visualization, writing, reviewing, and editing.

Majid Siavashi: Conceptualization, supervision, review and editing

Mohaddeseh Mousavi Nezhad: Methodology, conceptualization, writing, review and editing, supervision.

Alberto Guadagnini: Conceptualization, writing, review and editing, statistical approaches, and analysis.